Cement and Concrete Research 42 (2012) 313–320

Contents lists available at SciVerse ScienceDirect

Cement and Concrete Research

journal homepage: http://ees.elsevier.com/CEMCON/default.asp

Quantifying the effects of crack width, tortuosity, and roughness on water permeability of cracked mortars

Alireza Akhavan [a], Seyed-Mohammad-Hadi Shafaatian [a], Farshad Rajabipour [b,*]

[a] The Pennsylvania State University, Department of Civil and Environmental Engineering, University Park, PA 16802, USA
[b] The Pennsylvania State University, Department of Civil and Environmental Engineering, 223B Sackett Building, University Park, PA 16802, USA

ARTICLE INFO

Article history:
Received 16 June 2010
Accepted 6 October 2011

Keywords:
Crack detection (B)
Image analysis (B)
Durability (C)
Permeability (C)
Modeling (E)

ABSTRACT

The existing service-life prediction models rarely account for the effect of cracks on mass transport and durability of concrete. To correct this deficiency, transport in fractured porous media must be studied. The objective of this paper is to quantify the water permeability of localized cracks as a function of crack geometry (i.e., width, tortuosity, and surface roughness). Plain and fiber-reinforced mortar disk specimens were cracked by splitting tension; and the crack profile was digitized by image analysis and translated into crack geometric properties. Crack permeability was measured using a Darcian flow-thru cell. The results show that permeability is a function of crack width square. Crack tortuosity and roughness reduce the permeability by a factor of 4 to 6 below what is predicted by the theory for smooth parallel plate cracks. Although tortuosity and roughness exhibit fractal behavior, their proper measurement is possible and results in correct estimation of crack permeability.

1. Introduction

The permeability of concrete has an important impact on its durability since permeability controls the rate of penetration of moisture that may contain aggressive solutes and also controls moisture movement during heating and cooling or freezing and thawing [1]. While permeability of concrete is commonly measured using uncracked laboratory specimens [2,3], in real structures, the existence of cracks (induced by restrained shrinkage or mechanical loading) can significantly increase the penetration of moisture and salts into concrete. This can especially be significant for high strength concretes which are known to have a higher tendency for cracking due to a larger autogenous and thermal shrinkage and a lower capacity for stress relaxation [4,5,6]. As such, for service-life predictions, it is important to account for the effect of cracks on accelerating the transport of moisture and aggressive agents inside concrete. Unfortunately, the present generation of service-life models largely overlooks the effect of cracks on durability.

Research on the water permeability of crack-free concrete has been extensive [7,8,9,10,11,12] and has led to a general understanding that the saturated water permeability of concrete is a function of its porosity, pore connectivity, and the square of a threshold pore diameter [10,11,12]. In addition to the classical flow-thru permeability measurements [2,3], new methods (e.g., thermal expansion kinetics [13], beam bending [14], and dynamic pressurization [15]) have been offered that allow a more rapid and repeatable measurement of the saturated permeability.

In comparison, research on the permeability of cracked concrete has been limited. The pioneering works of Kermani [16], Tsukamoto and Wörner [17], and Gérard et al. [18] explored changes in permeability of concrete caused by the application of compressive or tensile stress. Wang et al. [19] measured the permeability of concrete disks fractured using a splitting tensile test, and correlated the crack opening displacement (COD) with the permeability coefficient of a crack. Their results suggested that for COD smaller than 25 μm, there is no significant increase in permeability beyond the matrix permeability. For larger cracks, permeability increases exponentially. It should be noted that in this study (as well as some future studies [20,21,22]), crack width was not directly measured; but assumed to be equal to the lateral displacement of the disk specimen which was measured using an LVDT setup (Fig. 1). This assumption could result in inaccuracies due to crack branching, variability of crack width along its length, and inelastic deformation of the matrix; as discussed later in this paper.

For use in service-life prediction models, it is important to establish a quantitative correlation between crack geometry and its permeability. Using the theory of laminar flow of incompressible Newtonian fluids inside a smooth parallel-plate gap, Eq. (1), often referred to as the Poiseuille law, can be derived showing that the water flow rate through a crack, Q (m^3/s), is related to the cube of crack width, b (m) [23]:

$$Q = \xi \frac{Lb^3}{12\eta}\left[\frac{dP}{dx}\right] \quad (1)$$

* Corresponding author. Tel.: +1 814 863 0601; fax: +1 814 863 7304.
E-mail addresses: aua211@psu.edu (A. Akhavan), sxs1071@psu.edu (S.-M.-H. Shafaatian), farshad@psu.edu (F. Rajabipour).

0008-8846/$ – see front matter © 2011 Elsevier Ltd. All rights reserved.
doi:10.1016/j.cemconres.2011.10.002

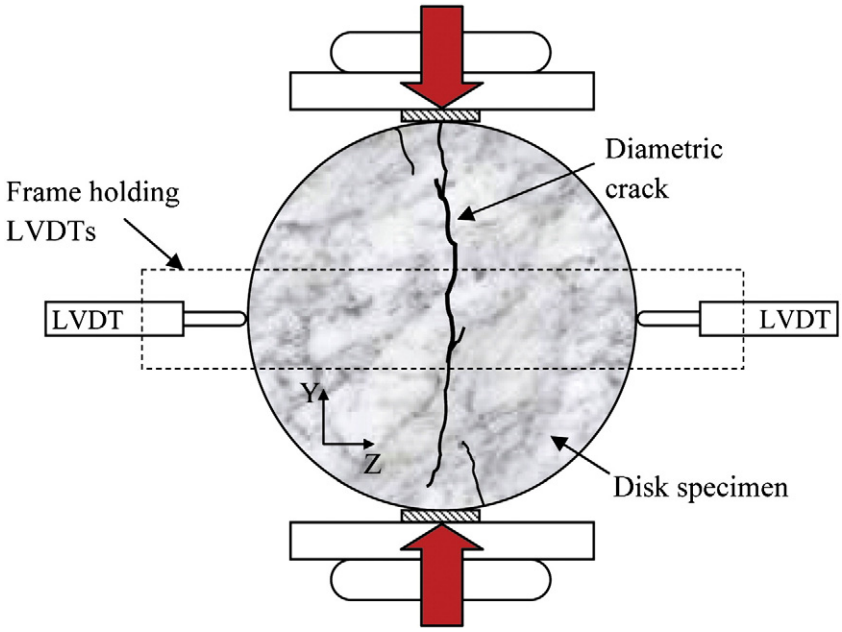

Fig. 1. Schematic illustration of the splitting tension setup used to fracture mortar disk specimens.

where Lb (m^2) is the crack cross sectional area perpendicular to the direction of flow, η (Pa·s) is dynamic viscosity of fluid, and $\left[\frac{dP}{dx}\right]$ (Pa/m) is the pressure gradient that drives the flow. This equation can be combined with Darcy's law:

$$J = \frac{Q}{Lb} = \frac{\kappa}{\eta}\left[\frac{dP}{dx}\right] \tag{2}$$

and alternatively presented in terms of the permeability coefficient of a crack κ (m^2), as a function of crack width square [24]:

$$\kappa = \xi\frac{b^2}{12}. \tag{3}$$

Eqs. (1) and (3) are strictly valid for a smooth, straight, and parallel plate crack. Real cracks in concrete never have such characteristics. As shown in Fig. 2, the crack width often varies along the length of a crack; cracks are tortuous meaning their actual length is larger than their nominal length; and crack wall surfaces are rough. These features reduce the permeability of a crack, sometimes significantly. To account for this reduction in permeability, in Eqs. (1) and (3), an empirical reduction factor ξ has been included; the values of $\xi = 0.001$ to 0.1 have been reported for plain and fiber reinforced concrete [21,25]. Unfortunately, these values are uncertain (vary several orders of magnitude), purely empirical, and have not been correlated to the geometric properties of cracks. For implementation in service-life models, it is important to improve the estimation of crack permeability (and other transport properties) as a function of crack geometric parameters; i.e., average or effective width, tortuosity, and roughness. The present paper pursues this objective.

2. Quantifying the geometric properties of cracks

2.1. Effective crack width

In a fractured disk specimen (Fig. 1), the actual crack profile is highly variable in both parallel and perpendicular dimensions with respect to the direction of the flow. In other words, the crack widths are variable both on the surface and through the thickness of the disk. For example, Fig. 3 shows the cumulative distribution function of crack widths on the surface of a mortar disk specimen. For comparison, the horizontal permanent displacement (after unloading), measured by LVDTs (Fig. 1), is also shown. It is clear that the LVDT reading is not a good measure of the actual crack profile or even the average crack width.

Using the digitized crack profile, an effective thru crack width, $b_{eff\text{-}thru}$, can be calculated that results in the same permeability coefficient as the actual variable crack. This is done by extension of a technique originally suggested by Dietrich et al. [26] for fractured rocks. The crack profile is discretized into a series of local parallel plates, which are further combined into a global parallel plate (Fig. 4). In Fig. 4(b), dimensions X, Y, and Z represent respectively

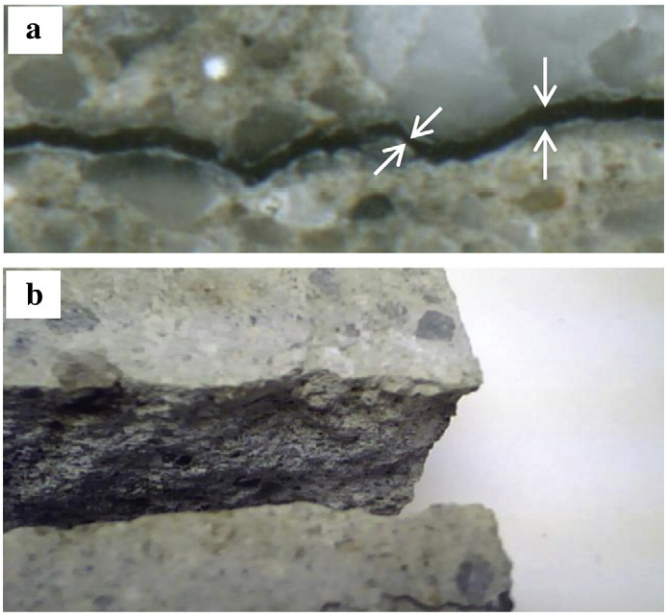

Fig. 2. A thru-thickness crack in a mortar disk specimen showing: (a) crack width variability and crack tortuosity, (b) crack wall roughness.

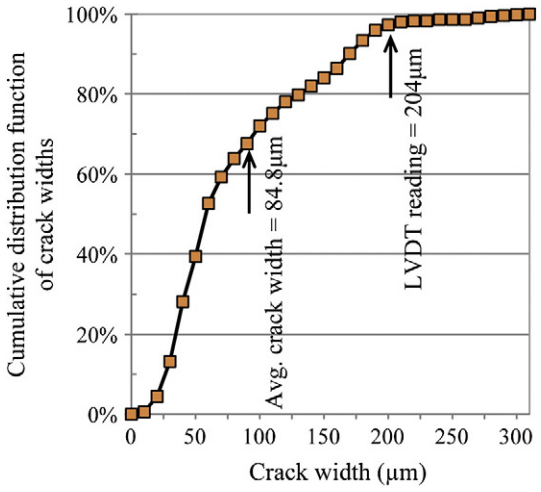

Fig. 3. Cumulative distribution function showing the variability of crack profile along the surface of a disk specimen.

the direction of the flow (e.g., thru thickness), diametric direction parallel to crack, and diametric direction perpendicular to crack (also see Fig. 1). If b_{ij} represent the crack width for the ith element in direction X and jth element in direction Y, the first row of elements can be represented by b_{1j}. To calculate an effective thru crack width, $b_{eff\text{-}thru}$, first, the effective crack for each row of elements is obtained ($b_{1,eff}$, $b_{2,eff}$, etc.). According to Darcy's law, for the first row of elements, the volumetric discharge rate ($Q_{1,T}$) is described as:

$$Q_{1,T} = \sum_{j=1}^{n} Q_{1j} = \frac{1}{\eta}\sum_{j=1}^{n} L_{1j} b_{1j} \kappa_{1j} \frac{\Delta P_{1j}}{d_{1j}} \tag{4}$$

where n is the number of elements in each row, and $\kappa_{1j} = \frac{b_{1j}^2}{12}$ and ΔP_{1j} represent the permeability and pressure loss for each element. Assuming that the elements' length and thickness are chosen constant: $L_{ij} = L$ and $d_{ij} = d$, and that the flow is 1-dimensional ($\Delta P_{11} = \Delta P_{12} = \ldots = \Delta P_1$):

$$Q_{1,T} = \frac{1}{12\eta}\frac{L}{d}\Delta P_1 \sum_{j=1}^{n} b_{1j}^3. \tag{5}$$

Combining Eq. (5) and Darcy's law results in:

$$Q_{1,T} = \frac{1}{12\eta}\frac{nL}{d}\Delta P_1 b_{1,\mathrm{eff}}^3 \tag{6}$$

$$b_{1,eff} = \sqrt[3]{\frac{1}{n}\sum_{j=1}^{n} b_{1j}^3}\,. \tag{7}$$

Eq. (7) can be used to determine the effective surface crack width at the top and bottom faces of each disk specimen (shown as $b_{eff\text{-}surf}$ in Fig. 6). To determine the effective thru crack width, $b_{eff\text{-}thru}$, a similar summation procedure is performed in the X direction. For a column of m crack elements with length, width, and thickness nL, $b_{i,eff}$, and d:

$$Q_T = Q_{1,T} = Q_{2,T} = \cdots = Q_{i,T} \tag{8}$$

$$\frac{1}{12\eta}\frac{nL}{md}\Delta P b_{\mathrm{eff}}^3 = \frac{1}{12\eta}\frac{nL}{d}\Delta P_1 b_{1,\mathrm{eff}}^3 = \cdots = \frac{1}{12\eta}\frac{nL}{d}\Delta P_i b_{i,\mathrm{eff}}^3 \tag{9}$$

where Q_T is the total discharge rate, $\Delta P = \Delta P_1 + \ldots + \Delta P_m$ is the total pressure loss across the specimen, and m is the number of rows. Simplification of Eq. (9) results in:

$$\Delta P_i = \Delta P_1 \left(\frac{b_{1,\mathrm{eff}}}{b_{i,\mathrm{eff}}}\right)^3 \tag{10}$$

$$\Delta P = \sum_{i=1}^{m} \Delta P_i = \Delta P_1 b_{1,\mathrm{eff}}^3 \sum_{i=1}^{m} \left(\frac{1}{b_{i,\mathrm{eff}}^3}\right) = m\Delta P_1 b_{1,\mathrm{eff}}^3 \left(\frac{1}{b_{\mathrm{eff}}^3}\right) \tag{11}$$

and ultimately:

$$b_{eff-thru} = \sqrt[3]{\frac{m}{\sum_{i=1}^{m}\left(\frac{1}{b_{i,\mathrm{eff}}^3}\right)}}. \tag{12}$$

2.2. Crack tortuosity and surface roughness

Fig. 5(a) and (b) show an actual thru-thickness crack profile and a schematic sketch of a crack to illustrate the methods used to quantify

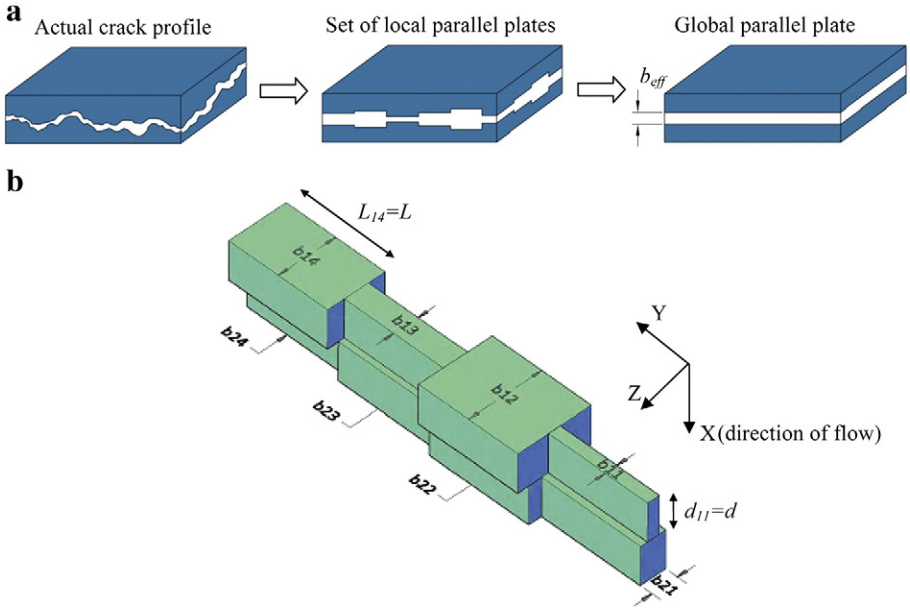

Fig. 4. Method for calculation of the effective crack width ((a) is redrawn and modified based on the image from Dietrich et al. [26]).

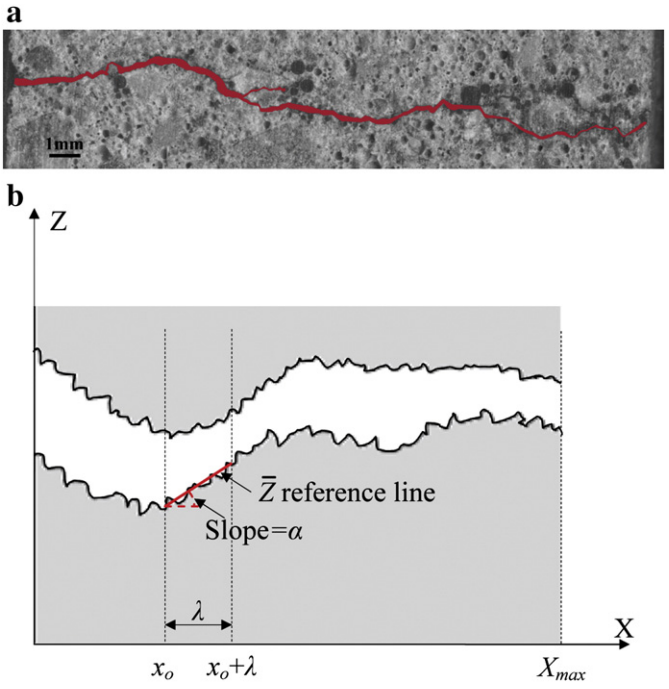

Fig. 5. (a) Digitized profile of an actual thru crack; (b) schematics of a crack profile to illustrate methods of quantifying tortuosity and roughness.

the tortuosity and roughness of crack. The crack profile is wavy (i.e., not straight) resulting in an effective crack length (L_e) larger than the nominal crack length X_{max}. The ratio:

$$\tau = \left(\frac{X_{max}}{L_e}\right)^2 \tag{13}$$

is known as the tortuosity factor. It has been shown [27] that permeability is reduced proportionally with $(X_{max}/L_e)^2$ and not with (X_{max}/L_e) since the larger effective length affects both pressure gradient and fluid velocity. In addition to tortuosity, the crack surfaces are rough which creates additional friction against the flow. Louis [28,29] suggested the following equation to estimate the permeability of a parallel-plate crack with rough walls in laminar flow:

$$\kappa = \frac{b^2}{12(1+8.8R_r^{1.5})} \tag{14}$$

where $R_r = R_a/2b$ is the relative surface roughness, and R_a (m) is the absolute roughness defined as the mean height of the surface asperities. This equation is empirical and valid for steady laminar flow with Reynolds number $R_e < 2300$ and rough crack surfaces with $R_r > 0.033$.

To quantify tortuosity and roughness, surface metrology techniques [30] can be employed. First, the surface profile is digitized and the x and z coordinates of all pixels on the crack surface are identified. The profile is then divided into segments of length λ. Within each segment, a reference $\bar{Z}$ line is drawn connecting the beginning and end points where the segment intersects the crack profile. The entire nominal length (X_{max}) is covered by n segments (note that n does not have to be integer) and the lengths of the reference $\bar{Z}$ lines are determined. By summation of the $\bar{Z}$ lengths, the effective length (L_e) is obtained and used for calculation of tortuosity. Note that L_e depends on the sampling length λ; smaller λ results in a longer L_e (more on this in Section 4.3).

Roughness is determined in two steps. First the segment $x=0$ to $x=\lambda$ is selected and its roughness is determined by calculating the average height of surface asperities with respect to its reference $\bar{Z}$ line:

$$R_{a,l} = \frac{1}{\lambda}\sum \left(|\bar{Z}(x) - Z(x)|\cos\alpha\right) \tag{15}$$

where $R_{a,l}$ (m) is the local roughness over this segment, and the quantity in front of Σ is the absolute value of the difference between crack profile and the reference line in the direction perpendicular to the reference line. Next, the segment is shifted 1 pixel to the right ($x=1$ to $x=\lambda+1$) and the local roughness is recalculated. The segment is swept over the entire assessment length ($x=0$ to $x=X_{max}$) and the corresponding $R_{a,l}$ values calculated. A total of $(X_{max}-\lambda)$ number of $R_{a,l}$ values are averaged to determine the global surface roughness:

$$R_{a,g} = \frac{1}{X_{max}-\lambda}\sum_{i=1}^{X_{max}-\lambda}\left(R_{a,l}\right)_i. \tag{16}$$

In addition, $R_{a,l}$ values obtained can be used to construct a probability density function for the surface roughness of the crack. The roughness can be measured using the top, bottom or both crack surfaces. Note that $R_{a,l}$ and $R_{a,g}$ will depend on the sampling length λ (more on this in Section 4.3). In this study, the procedures for measurement of tortuosity and roughness, as described above, were executed automatically through a MATLAB programming code.

3. Materials and experiments

3.1. Sample preparation

Disk-shape plain and fiber-reinforced mortar specimens were prepared, diametrically fractured, and tested for permeability. The mortar mixture proportions are provided in Table 1. Type I/II Portland cement (per ASTM C150-07), natural glacier sand (meeting the gradation requirements of ASTM C33-07), and polypropylene fibers (8 mm length, 39 μm diameter, vol. fraction 1%) were used. Disks (8.9 cm diameter × 2.5 cm thickness) were cut from 17.8 cm tall mortar cylinders after 28 days of moist curing. The disks were fractured using a deformation controlled splitting tensile test (Fig. 1). Vertical load was applied using a Universal Testing Machine by maintaining a constant rate of vertical deformation at 1 μm/s. The horizontal displacement was continuously monitored using two LVDTs positioned at the opposite sides of the specimen. As each specimen approached its peak load, a localized vertical crack formed starting from the middle section of the disk and growing outwards. After reaching a desired horizontal displacement, each specimen was unloaded at a vertical displacement rate of 5 μm/s. Various average crack widths in the range 10 to 200 μm were generated using this procedure. After fracturing, specimens were wrapped in plastic covers and kept in a moist room until they were due for permeability test. Each disk was vacuum saturated inside saturated $Ca(OH)_2$ solution for 24 h prior to the permeability test.

Table 1
Mixture proportions for mortar specimens.

Component	Proportions (kg/m^3)	
	Plain	Fiber-reinforced
Cement	600	600
Sand	1375	1375
Water	270	270
Fiber	–	7.5
Stabilizing admixture	–	0.9
Water reducing admixture	3.25	3.25

3.2. Permeability measurement

The saturated permeability was measured using a Darcian flow-thru cell and according to the procedure of CRD-C48-92. Inside a stainless steel cell, a disk specimen was securely seated on a retainer ring bonded to the specimen using a layer of high strength plaster. The circumferential surface of the specimen was sealed using a 70/30 mixture of paraffin and rosin. A layer of silicone sealant was applied on the top to seal the steel–wax interface. The silicon was allowed to cure for 4 h while the top surface of the specimen was kept wet to prevent drying of the mortar. The permeability test was performed using a pressure gradient of 68.9 kPa (10 psi). This resulted in a laminar flow with Reynolds numbers smaller than 118. The input water was pressurized by air inside a bladder, and this pressure was constantly monitored during the test. The output water was at atmospheric pressure. The outflow was collected inside a volumetric flask placed on top of a digital balance with accuracy 0.01 g. Weight measurements were performed automatically by a computer at 10 s intervals. To prevent evaporation of outflow water, the mouth of the volumetric flask was sealed with adhesive plastic with a small puncture to allow pressure equilibrium. Further, the water inside the flask was covered with a thin layer of oil.

Past research has shown that due to a self-healing phenomenon, permeability of cracks continuously decreases during the test [31,32,33]. The crack healing during the permeability test has been attributed to carbonation of concrete and formation of calcite ($CaCO_3$), renewed hydration of cement, and/or dissolution and re-deposition of portlandite ($Ca(OH)_2$). The results of the current study show up to 85% reduction in crack permeability during the first 24 h of the experiment, with narrower cracks showing a higher reduction than wider cracks. To maintain consistency, it was decided to use the outflow rate at 15 min to determine the permeability of cracks. The 15-min water flux inside cracks of various widths was measured as 3 to 53 cm/s. Considering the specimens thickness (2.5 cm), the measured flux values suggest that cracks are fully saturated within the first few seconds of the test. It should be noted that the matrix permeability is several orders of magnitude smaller than crack permeability (see Fig. 8), and as such, the exact degree of saturation of the matrix has little effect on the crack permeability measurements. Nevertheless, to maintain the specimen as close as possible to full saturation, each specimen had been vacuum saturated for 24 h in $Ca(OH)_2$ solution before the permeability test was initiated.

It should be further noted that due to self-healing, crack geometry (i.e., width, tortuosity, and roughness) is constantly changing during the test, and its effect is reflected as a reduction in permeability. The purpose of this study is to find a quantitative correlation between crack geometry and its permeability. As such, it was decided to terminate the test immediately after the measurement of permeability (15 min), to be able to capture the crack geometry that corresponds with the value of measured permeability.

3.3. Measuring crack dimensions

Immediately after permeability measurement, the specimen was taken out of the cell, cleaned and air dried for 24 h (23 °C, 50% RH). It should be noted that some changes in the crack width may be inevitable due to drying shrinkage. The crack dimensions were measured using digital image analysis. To reach higher contrast between the crack and the matrix, specimens were vacuum impregnated with a low viscosity black epoxy for 15 min. After epoxy hardened, the specimen's top and bottom faces were polished to remove the surface layer of epoxy and obtain flat surfaces. Next, the crack profile on the top and bottom faces was scanned using a digital scanner with resolution 9600 dpi (i.e., pixel size ≈ 2.65 μm). This results in a crack detection limit of approximately 5.3 μm (i.e., 2 pixels wide). The surface crack width was measured every 200 μm along the diametric crack, and the results were used to obtain the effective surface crack width $b_{eff\text{-}surf}$ (Eq. (7)).

In addition to crack width measurements along the top and bottom surfaces of each disk, three plain and five fiber-reinforced specimens were vertically sectioned at the mid-point along a diameter perpendicular to the surface crack and the crack profile through the specimen's thickness was scanned (Fig. 6). The thru crack widths were measured every 50 μm, and the results were used to obtain the effective thru crack width $b_{eff\text{-}thru}$ using Eq. (12). To be able to calculate the effective thru crack width for the entire specimen, the possibility of establishing a correlation between the effective surface and the effective thru crack widths was explored. For the eight specimens vertically sectioned, the effective thru crack width was calculated along each section. Also, the effective surface crack width corresponding to each section was calculated. The portion of surface crack between 0.375 and 0.625 points was assumed to correspond with the middle thru section (Fig. 6). Fig. 6 shows a linear correlation between the effective surface and thru crack widths obtained for both plain and fiber-reinforced specimens. It should be noted that this correlation is not universal and may be different for other materials or cracks developed by other loading conditions. Strictly speaking, it should only be applied to the mortar specimens tested in this work; for other materials, verification is needed. Here this correlation is used only to translate the effective surface crack width (calculated by scanning the crack at top and bottom surfaces of specimen) into an effective thru crack width for specimens tested in this study. It should be noted that alternatively, 3D tomography techniques (e.g., X-ray CAT) can be used to obtain the three dimensional crack profile [34]. However, the resolution of such measurements can be a limiting factor. For commonly available X-ray tomography instruments, the resolution is on the order of 1/1000 of the sample dimension (e.g., 89 μm for 89 mm diameter specimens).

4. Results and discussion

4.1. Comparison between average, effective, and LVDT crack measurements

A total of 20 plain and fiber-reinforced disk specimens were fractured and tested in this study. Fig. 7 shows comparisons among the average and effective crack widths and LVDT measurements. The average and effective crack widths are closely correlated with the effective thru crack widths approximately 13% larger than the average surface crack widths. This may suggest that when the average crack width is properly determined from the specimens' surfaces, the effective crack width can be estimated with a reasonable accuracy without

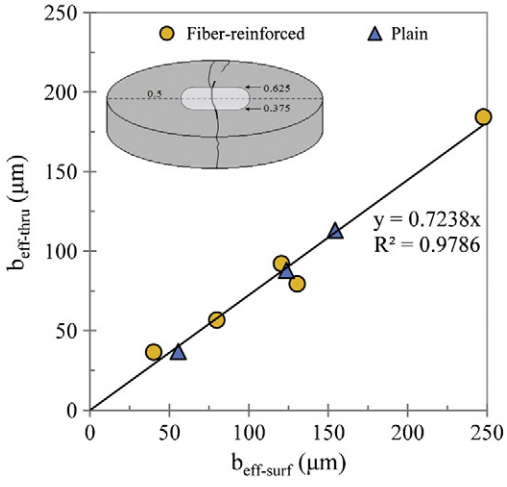

Fig. 6. Correlation between the effective surface and thru crack widths.

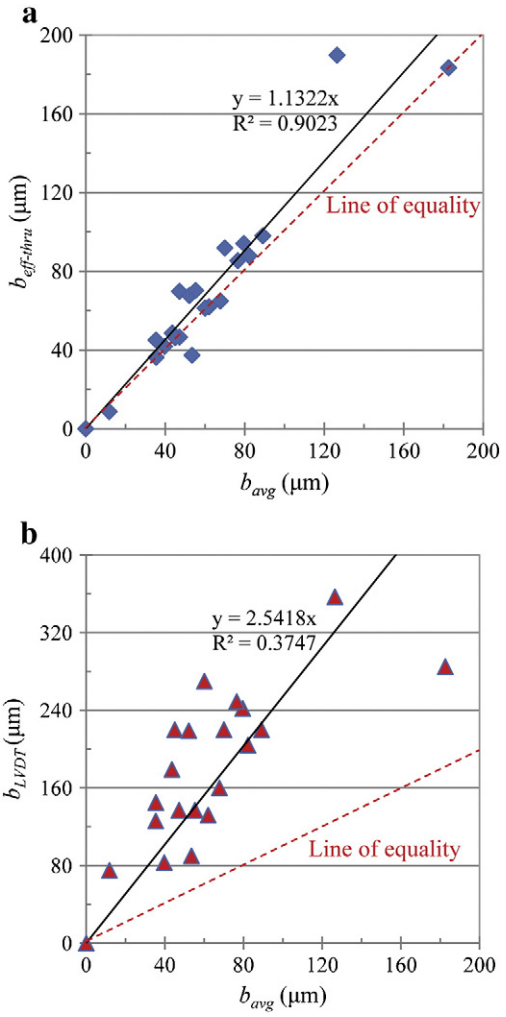

Fig. 7. Correlation between (a) average and effective crack widths, (b) average crack width and LVDT readings.

the need to slice the specimens or perform calculations described by Eqs. (7) and (12).

In comparison, the LVDT measurements show a significant scatter while they are consistently over-estimating the crack widths, approximately by a factor 2.5. This again suggests that horizontal LVDT measurements must not be used to estimate crack widths in a splitting tensile test.

4.2. Saturated permeability as a function of crack width

The results of experimental measurements of crack permeability for plain and fiber-reinforced mortars are presented in Fig. 8. For comparison, the values predicted by the parallel plate theory ($\kappa = b^2/12$) are also included. The curves present the best fit of Eq. (3) to the experimental and theoretical data. For the experimental data, the best ξ corresponding to the least error was determined. Several important observations can be made. (1) The permeability of cracks is more than 6 orders of magnitude larger than the matrix permeability. (2) The experimental results agree with the trend predicted by the theory. In other words, crack permeability is a function of crack with square. (3) However, the experimental values of permeability are smaller than the theory by a factor of 4 to 6. The best fit for the plain specimens results in $\xi = 0.229$ and for the fiber-reinforced specimens $\xi = 0.163$. This could be due to crack tortuosity, and the friction caused by crack's surface roughness and presence of fibers. (4) The experimental results exhibit a considerable scatter. While a coefficient of variation of 65% has been reported for single-operator

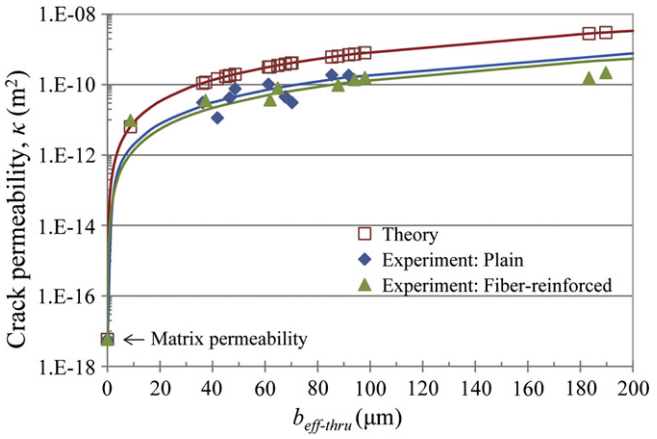

Fig. 8. Theoretical and experimental values of crack permeability as a function of effective crack width.

permeability measurement of uncracked concrete [35], the existence of cracks can further contribute to scattering of results due to crack branching and variability of crack profile in three dimensions. Future research can explore the precision in permeability measurement of less variable cracks (e.g., manufactured gaps with certain thickness and surface roughness).

4.3. Crack tortuosity and surface roughness

It is known that fracture surfaces exhibit fractal behavior [36]. This means that crack profile looks similarly tortuous and jagged at different scales of magnification (a property called self-similarity). Examples of fractal functions are numerous in nature including mountains, coastlines, clouds, plants, and natural and manufactured surfaces. The fractal nature of cracks in concrete materials has been recognized by earlier researchers [37,38,39,40] who attempted to link the surface area and roughness of cracks to the fracture toughness of the material. A similar approach can be adopted to relate the tortuosity and roughness of cracks to their transport properties.

Fig. 9(a) shows the effective length (L_e) of a thru-thickness crack, in a fiber-reinforced specimen, measured using significantly different values of sampling length scale (λ) as per Section 2.2. The crack had a nominal length $X_{max} = 20.66$ mm. It is observed that the measured values of L_e depend strongly on λ and increase from 22.40 mm at $\lambda = 12{,}755$ μm to 49.19 mm at $\lambda = 3.8$ μm. This represents a change in the tortuosity factor from $\tau = 0.85$ to 0.18 (i.e., becoming considerably more tortuous at smaller λs). Despite its significant dependence on λ, L_e can be considered a statistically self-similar fractal only if it follows the power function [36]:

$$L_e = F\lambda^{1-D} \tag{17}$$

where D (−) is the fractal dimension and F (m) is a constant. This power function shows as a straight line on a log–log scale which fits well to the data reported in Fig. 9(a), and results in a fractal dimension $D = 1.095$. A comparison between the measured L_e values from two cracks in a plain and a fiber-reinforced specimen is provided in Fig. 9(b). The plain crack shows similar or slightly smaller L_e values (i.e., less tortuous crack) depending on the measurement's length scale (λ). The fractal dimension of the plain crack was determined as $D = 1.096$. Similar results were obtained by analyzing other thru-thickness cracks in plain and fiber-reinforced specimens.

In addition, the global roughness of the plain and fiber-reinforced thru cracks was measured based on the procedure of Section 2.2. The results are presented in Fig. 10. Unlike the effective length (L_e), which increases for smaller λs, the crack roughness decreases monotonically as λ decreases. This is anticipated since at smaller sampling length

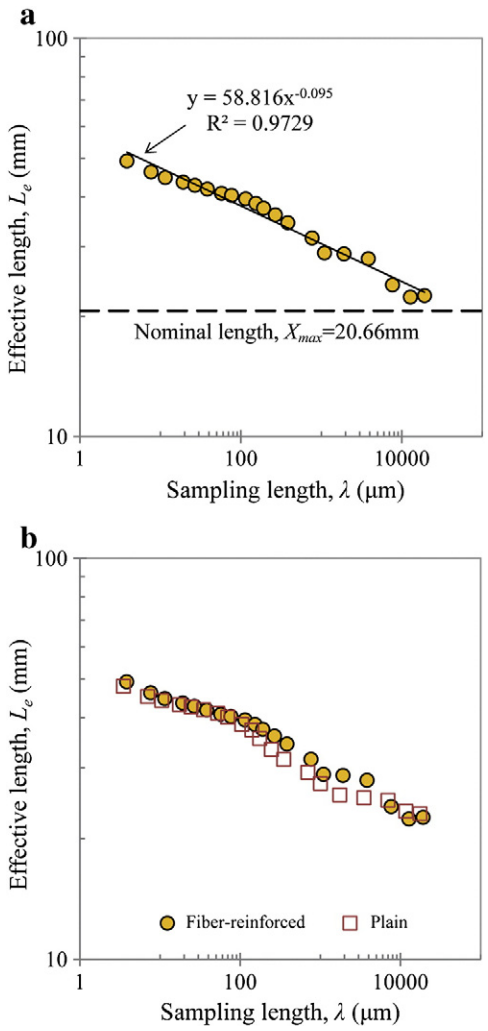

Fig. 9. Effective crack length as a function of sampling length scale: (a) fiber-reinforced crack fitted by a fractal power function; (b) comparison between plain and fiber-reinforced cracks.

scales, crack shows smaller surface features. Except for very large values of λ, the crack roughness shows a strong self-similar fractal behavior that can be represented by the power function [41]:

$$R_{a,g} = F\lambda^{2-D}. \tag{18}$$

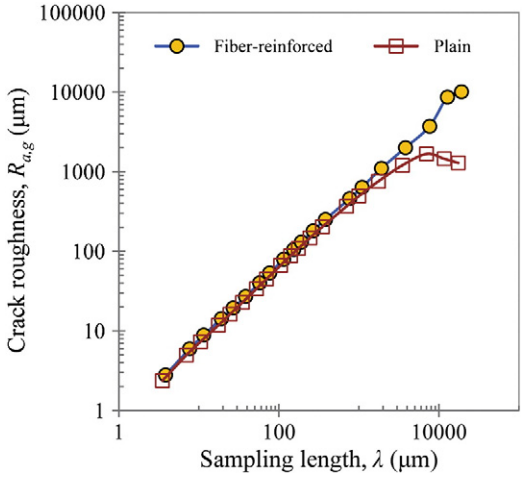

Fig. 10. Crack surface roughness as a function of sampling length scale.

Table 2
Average tortuosity and roughness measured using different values of λ.

λ (μm)	τ (−)	$R_{a,g}$ (μm)
1000	0.51	637
100	0.27	70
10	0.21	8.9

The fractal dimensions of $D = 1.085$ and $D = 1.052$ were obtained for the plain and fiber-reinforced cracks. Further, the presence of fibers does not show a measurable impact on the roughness of cracks.

4.4. Effect of tortuosity and roughness on crack permeability

Table 2 shows the average values (between plain and fiber-reinforced specimens) of crack tortuosity factor and surface roughness measured using different values λ. These values can be used, along with the effective or average crack width, to estimate crack permeability using Louis Eq. (14) that has been modified by adding the tortuosity factor:

$$\kappa = \frac{\tau b^2}{12\left(1 + 8.8R_r^{1.5}\right)}. \tag{19}$$

The results are presented in Fig. 11 which compares the estimated permeability from Eq. (19) with values measured by experiment. Among the three estimate curves, the one corresponding to $\lambda = 10$ μm ($\tau = 0.21$, $R_{a,g} = 8.9$ μm) matches the best to experimental data. This underlines the significance of choosing a proper sampling length for estimation of crack tortuosity and roughness. The observations from Fig. 11 suggest that the sampling length must be several times smaller than the width of the examined crack. Further, Eq. (19) can provide a good quantitative estimate of crack permeability, at least for the effective crack widths in the range 35 to 100 μm. Future research should examine the applicability of this equation for cracks of different size and in concrete materials other than the specific mortars studied in this work.

5. Conclusions

Based on the results of this research, the following conclusions can be drawn:

- Using a digitized crack profile, an effective crack width can be calculated that results in the same permeability as the actual crack whose width is variable along its length. The effective crack width shows a reasonably good correlation with the arithmetic average of crack widths. On the other hand, horizontal displacement of disk specimen during the splitting tensile test (i.e., LVDT reading) does not correlate

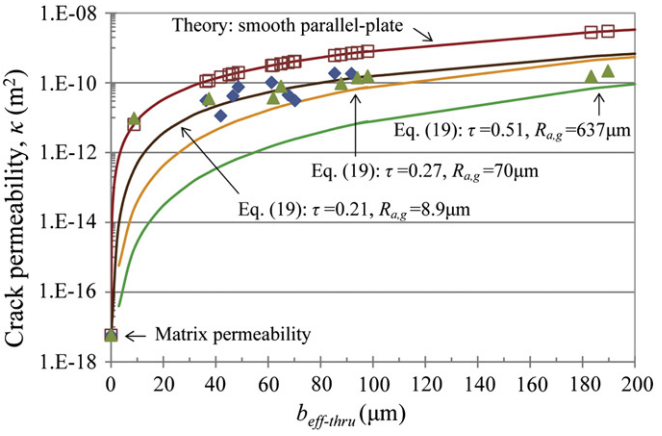

Fig. 11. Estimation of crack permeability based on Eq. (19); data points show experimental results.

well with average or effective crack width and should not be used to estimate crack dimensions.

- Experimental measurements show that crack permeability coefficient is a function of crack width square. While this trend agrees with the theory of laminar flow in smooth parallel plat gaps, the measured permeability values are smaller than the theory by a factor 4 to 6 due to tortuosity and surface roughness of cracks.
- Tortuosity and surface roughness of cracks exhibit fractal behavior. In other words, the numerical values of these parameters depend significantly on the magnification of length scale. In this work, plain and fiber-reinforced cracks were examined at several different length scales from μm to mm. Both tortuosity and roughness show a statistically self-similar fractal behavior across these length scales, with fractal dimensions measured in the range 1.052 to 1.096.
- Towards the main objective of this work, a modification of the Louis equation by adding a tortuosity factor was found to be capable of quantifying crack permeability as a function of crack geometry (i.e., width, tortuosity, and surface roughness). Tortuosity and roughness of crack must be measured using a sampling length scale that is several times smaller than crack width.

Acknowledgments

The authors would like to thank Profs. S.P. Shah, H-W. Reinhardt, G.W. Scherer, and J. Weiss for their discussions and insightful comments. This work was conducted at the CITEL laboratory of Penn State and the Materials and Structures laboratory of the University of Hawaii; the authors acknowledge the support that has made these laboratories operational.

References

[1] S. Mindess, J.F. Young, D. Darwin, Concrete, 2nd ed. Prentice Hall, Upper Saddle River, New Jersey, 2003.
[2] CRD-C48-92, Standard test method for water permeability of concrete, Handbook of Cement and Concrete, US Army Corps of Engineers, 1992.
[3] ASTM D 5084-03, Standard Test Methods for Measurement of Hydraulic Conductivity of Saturated Porous Materials Using a Flexible Wall Permeameter, American Society for Testing and Materials, West Conshohocken, Pennsylvania, 2003.
[4] P.D. Krauss, E.A. Rogalla, Transverse Cracking in Newly Constructed Bridge Decks, NCHRP Report No. 380, Transportation Research Board, Washington, D.C., 1996
[5] D. Darwin, J. Browning, W.D. Lindquist, Control of cracking in bridge decks: observations from the field, Cement Concrete Aggr. 26 (2004) 148–154.
[6] ACI 231R-10, Report on Early-Age Cracking: Causes, Measurement and Mitigation, American Concrete Institute, Farmington Hills, Michigan, 2010.
[7] A.S. El-Dieb, R.D. Hooton, Water-permeability measurement of high performance concrete using a high-pressure triaxial cell, Cem. Concr. Res. 25 (1995) 1199–1208.
[8] D. Ludirdja, R.L. Berger, J.F. Young, Simple method for measuring water permeability of concrete, ACI Mater. J. 86 (1989) 433–439.
[9] T.C. Powers, L.E. Copeland, J.C. Hayes, H.M. Mann, Permeability of portland cement paste, J. Am. Concrete Inst. 51 (1954) 285–298.
[10] A.J. Katz, A.H. Thompson, Quantitative prediction of permeability in porous rock, Phys. Rev. B 34 (1986) 8179–8181.
[11] P. Halamickova, R.J. Detwiler, D.P. Bentz, E.J. Garboczi, Water permeability and chloride ion diffusion in portland cement mortars: relationship to sand content and critical pore diameter, Cem. Concr. Res. 25 (1995) 790–802.
[12] M.R. Nokken, R.D. Hooton, Using pore parameters to estimate permeability or conductivity of concrete, Mater. Struct. 41 (2008) 1–16.
[13] H. Ai, J.F. Young, G.W. Scherer, Thermal expansion kinetics: method to measure permeability of cementitious materials: II, application to hardened cement pastes, J. Am. Ceram. Soc. 84 (2001) 385–391.
[14] G.W. Scherer, Measuring permeability of rigid materials by a beam-bending method: I, theory, J. Am. Ceram. Soc. 83 (2000) 2231–2239.
[15] Z.C. Grasley, G.W. Scherer, D.A. Lange, J.J. Valenza, Dynamic pressurization method for measuring permeability and modulus: II. Cementitious materials, Mater. Struct. 40 (2007) 711–721.
[16] A. Kermani, Permeability of stressed concrete, Build. Res. Inform. 19 (1991) 360–366.
[17] M. Tsukamoto, J.-D. Wörner, Permeability of cracked fibre-reinforced concrete, Darmstadt Concrete Annu. J. Concrete Concrete Struct. 6 (1991) 123–135.
[18] B. Gérard, D. Breysse, A. Ammouche, O. Houdusse, O. Didry, Cracking and permeability of concrete under tension, Mater. Struct. 29 (1996) 141–151.
[19] K. Wang, D.C. Jansen, S.P. Shah, Permeability study of cracked concrete, Cem. Concr. Res. 27 (1997) 381–393.
[20] C.-M. Aldea, S.P. Shah, A. Karr, Effect of cracking on water and chloride permeability of concrete, ASCE J. Mater. Civil Eng. 11 (1999) 181–187.
[21] V. Picandet, A. Khelidj, H. Bellegou, Crack effect on gas and water permeability of concrete, Cem. Concr. Res. 39 (2009) 537–547.
[22] S.Y. Janga, B.S. Kimb, B.H. Oh, Effect of crack width on chloride diffusion coefficients of concrete by steady-state migration tests, Cem. Concr. Res. 41 (2011) 9–19.
[23] B. Massey, J. Ward-Smith, Mechanics of Fluids, 8th ed. Taylor & Francis, London, 2006.
[24] D. Snow, Anisotropic permeability of fractured media, Water Resour. Res. 5 (1969) 1273–1289.
[25] J.-P. Charron, E. Denarié, E. Brühwiler, Transport properties of water and glycol in an ultra high performance fiber reinforced concrete (UHPFRC) under high tensile deformation, Cem. Concr. Res. 38 (2008) 689–698.
[26] P. Dietrich, R. Helming, M. Sauter, H. Hötzl, J. Köngeter, G. Teutsch, Flow and Transport in Fractured Porous Media, Springer, Berlin, 2005.
[27] J. Bear, Dynamics of Fluids in Porous Media, Dover Publications, New York, 1988.
[28] G. de Marsily, Quantitative Hydrogeology, Academic Press, San Diego, 1986.
[29] C. Louis, Section III, Introduction à l'hydraulique des roches, Bull BRGM Série 2, vol. 4, 1974, pp. 283–356, (in French).
[30] D. Whitehouse, Surfaces and Their Measurement, Taylor and Francis, New York, 2002.
[31] N. Hearn, Self-sealing, autogenous healing, and continuous hydration: what is the difference? Mater. Struct. 31 (1998) 563–567.
[32] C. Edvartsen, Water permeability and autogenous healing of cracks in concrete, ACI Mater. J. 96 (1999) 448–454.
[33] H.-W. Reinhardt, M. Jooss, Permeability and self-healing of cracked concrete as a function of temperature and crack width, Cem. Concr. Res. 33 (2003) 981–985.
[34] A.S. Poupeleer, J. Carmeliet, S. Roels, D. van Gemert, Determination of the ion diffusion coefficient of cracked porous media, in: J. Carmeliet, H. Hens, G. Vermeir (Eds.), Research in Building Physics, Swets & Zeitlinger, Lisse, The Netherlands, 2003.
[35] A. Bhargava, N. Banthia, Permeability of concrete with fiber reinforcement and service-life predictions, Mater. Struct. 41 (2007) 363–372.
[36] B.B. Mandelbrot, The Fractal Geometry of Nature, W.H. Freeman and Company, New York, 1983.
[37] V.E. Saouma, C.C. Barton, N.A. Gamaleldin, Fractal characterization of fracture surfaces in concrete, Eng. Fract. Mech. 35 (1/2/3) (1990) 47–53.
[38] D.A. Lange, H.M. Jennings, S.P. Shah, Relationship between fracture surface roughness and fracture behavior of cement paste and mortar, J. Am. Ceram. Soc. 76 (3) (1993) 589–597.
[39] T. Ficker, D. Martišek, H.M. Jennings, Roughness of fracture surfaces and compressive strength of hydrated cement pastes, Cem. Concr. Res. 40 (2010) 947–955.
[40] M.A. Issa, A.M. Hammad, A. Chudnovsky, Correlation between crack tortuosity and fracture toughness in cementitious materials, Int. J. Fract. 60 (1993) 97–105.
[41] J.C. Russ, Fractal Surfaces, Plenum Press, New York, 1994.